# Characterisation of transverse turbulent motion in quasi-two-dimensional aerated flow: Application of four-point air-water flow measurements in hydraulic jump

Hang Wang*, Hubert Chanson

*The University of Queensland, School of Civil Engineering, Brisbane, QLD 4072, Australia*

## ABSTRACT

The measurement of turbulent velocity in highly aerated flow is difficult because of the presence of air bubbles. The characterisation of three-dimensional velocity field in highly aerated flows is even more challenging using existing phase-detection techniques. This paper presents an attempt on a quantification of transverse velocity and velocity fluctuations in quasi-two-dimensional hydraulic jumps with relatively high Froude and Reynolds numbers. A four-sensor phase-detection probe array was developed to measure the bubble convection in both streamwise and spanwise directions. A characteristic instantaneous transverse velocity component was derived together with a measure of its fluctuations. The transverse velocity component characterised the three-dimensional turbulent structures, although the time-averaged flow pattern was two-dimensional and the average transverse velocity was zero. Both the transverse velocity and velocity fluctuations were smaller than the longitudinal time-averaged velocity and velocity fluctuations in the shear flow, and were quantitatively comparable to those in the free-surface region, revealing different turbulent structures in the lower and upper roller regions. The approximate of Reynolds stresses was discussed together with the limitation of the method. The present work also provided some guidelines for the use of phase-detection probe array and correlation signal processing techniques in complex turbulent two-phase flows.

## 1. Introduction

A rapidly-varied open channel flow in a prismatic flume is commonly treated as a two-dimensional flow, although three-dimensional flow patterns are often observed associated with the development of large-scale turbulent structures and secondary flow at the rapid flow transition [14,30]. A canonical case is a hydraulic jump. Fig. 1A and B show respectively a hydraulic jump in a natural stream and an artificial jump in a horizontal rectangular channel. While the former exhibits a three-dimensional flow pattern with a curved impingement perimeter, the latter is considered to have a zero average flow motion in the horizontal transverse direction perpendicular to the channel centreline.

Experimental characterisation of three-dimensional flow field becomes extremely difficult with the occurrence of air entrainment and intense interactions between the entrained air bubbles and turbulent structures [16]. Most classic velocity measurement techniques such as laser Doppler velocimetry (LDV), acoustic Doppler velocimetry (ADV) and particle image velocimetry (PIV) are adversely affected by the presence of air-water interfaces [1], thus their applications in hydraulic

jumps were restricted in weak jumps at low Reynolds numbers with very-low air content levels [18,19,22,23,34]. For highly-aerated flows, the largest number of and most successful air-water flow measurements in the past decades were conducted with intrusive phase-detection probes [4,9]. The phase-detection probe is a local point-measurement technique. In addition to local void fraction and bubble characteristics, time-averaged interfacial velocity can be quantified using a dual-tip probe between two conductivity or optical fibre sensors in the streamwise direction [10,28,35]. The development of bubbly flow imaging techniques also allowed for a depiction of two-dimensional velocity field in a longitudinal-vertical visualisation plane, although the bubble diffusion and velocity distribution may be distorted by the lateral boundary layer next to the observation window, and no information in the transverse direction is available [2,3,17,25].

Measurement of air-water flow turbulence properties in the spanwise direction may involve multi-point measurements, although application in high-speed open channel flows was rare [21,26]. For the particular case of highly-aerated hydraulic jumps, measure of transverse flow structures was investigated in terms of the integral turbulent

---

(a)



(b)



**Fig. 1.** Photographs of hydraulic jumps: (a) A three-dimensional hydraulic jump in a natural waterway. Flow from left to right. January 2016 in Taiwan; (b) An experimental hydraulic jump in a horizontal rectangular channel. Flow rate 0.0347 m³/s, channel width 0.5 m, inflow length 0.83 m, inflow depth 0.0206 m, inflow velocity 3.37 m/s, inflow Froude number 7.5, inflow Reynolds number $6.8 \times 10^4$. Flow from left to right with partially-developed inflow conditions. November 2015 at The University of Queensland.

length and time scales based upon correlation analyses. These included the evaluation of turbulent scales of the free-surface fluctuations [6,29] and the internal bubbly flow structures [37,38]. These findings indicated different longitudinal and transverse dimensions of coherent bubbly structures in a close region downstream of the jump toe. However, the only physical measurement of transverse velocity fluctuations in the highly-aerated air-water flow region of hydraulic jumps that the authors are aware of by far is the work of Resch and Leutheusser [32] using hot-film anemometers. Their study also emphasised the significance of inflow conditions (fully- or partially-developed incident flow) influencing the turbulence development downstream of the jump toe. Although three-dimensional numerical modelling exhibited the potential to provide more information about the flow dynamics [20,24], the simulation of bubble entrainment process at large Reynolds numbers is still a major challenge, preventing successful verification and validation of any existing numerical models against physical data obtained in relatively strong hydraulic jumps.

It is the aim of the present study to develop a new method to evaluate the transverse velocity fluctuations in turbulent air-water flows, especially in the highly-aerated flow regions where the traditional monophasic flow measurement techniques are not applicable. Hydraulic jumps with large Froude and Reynolds numbers were selected as the investigated flows, and the instrumentation consisted of an array of four conductivity phase-detection sensors. The streamwise and spanwise transport of air-water interfaces was measured in a horizontal plane, and the velocity components were derived including a characteristic instantaneous transverse component and its fluctuations. The shear stresses were preliminarily discussed, followed by a discussion of the limitation of this newly-developed technique.

## 2. Experimental facility, instrumentation and flow conditions

Hydraulic jumps were produced in a 3.2 m long, 0.5 m wide and 0.4 m deep horizontal rectangular channel (Figs. 1B and 2A). The channel was built with a smooth HDPE bed and glass sidewalls. Water was discharged into the channel from an upstream head tank with the same width. The head tank was equipped with a series of flow straighteners and a rounded undershoot gate (Ø = 0.3 m) that induced a horizontal impinging flow without contraction. The longitudinal position of hydraulic jump was controlled by an overshoot gate located at the downstream end of the channel. Fig. 2A illustrates the experimental facility setup, where $x$ is the longitudinal coordinate originating from the upstream gate and positive downstream, $y$ is the vertical coordinate originating from the channel bed and positive upward, and $z$ is the transverse coordinate with $z = 0$ on the channel centreline.

The flow rate $Q$ was measured with a Venturi meter installed along the supply pipeline with an expected accuracy of $\pm$ 2%. The clear water depth $d_1$ upstream of the jump toe was measured with a pointer gauge, the accuracy being determined between 0.2 mm (accuracy of the pointer gauge) and the inflow surface roughness which was a function of $d_1$ and the inflow Froude number. An ultra-high-speed camera (Phantom v2011) was used for general observations of two-dimensional velocity distributions in the $x$-$y$ plane against the transparent channel sidewall. Full-resolution (1280 × 800 pixels) movies were recorded at 22,600 fps for 1.5 s, with an actual observation window size of $0.64 \times 0.4$ m². The time-averaged velocity was analysed based on an optical flow visualisation technique that recovered the global apparent motion of the moving fluid through consecutive pairs of recorded images by application of a local gradient-based method [39].
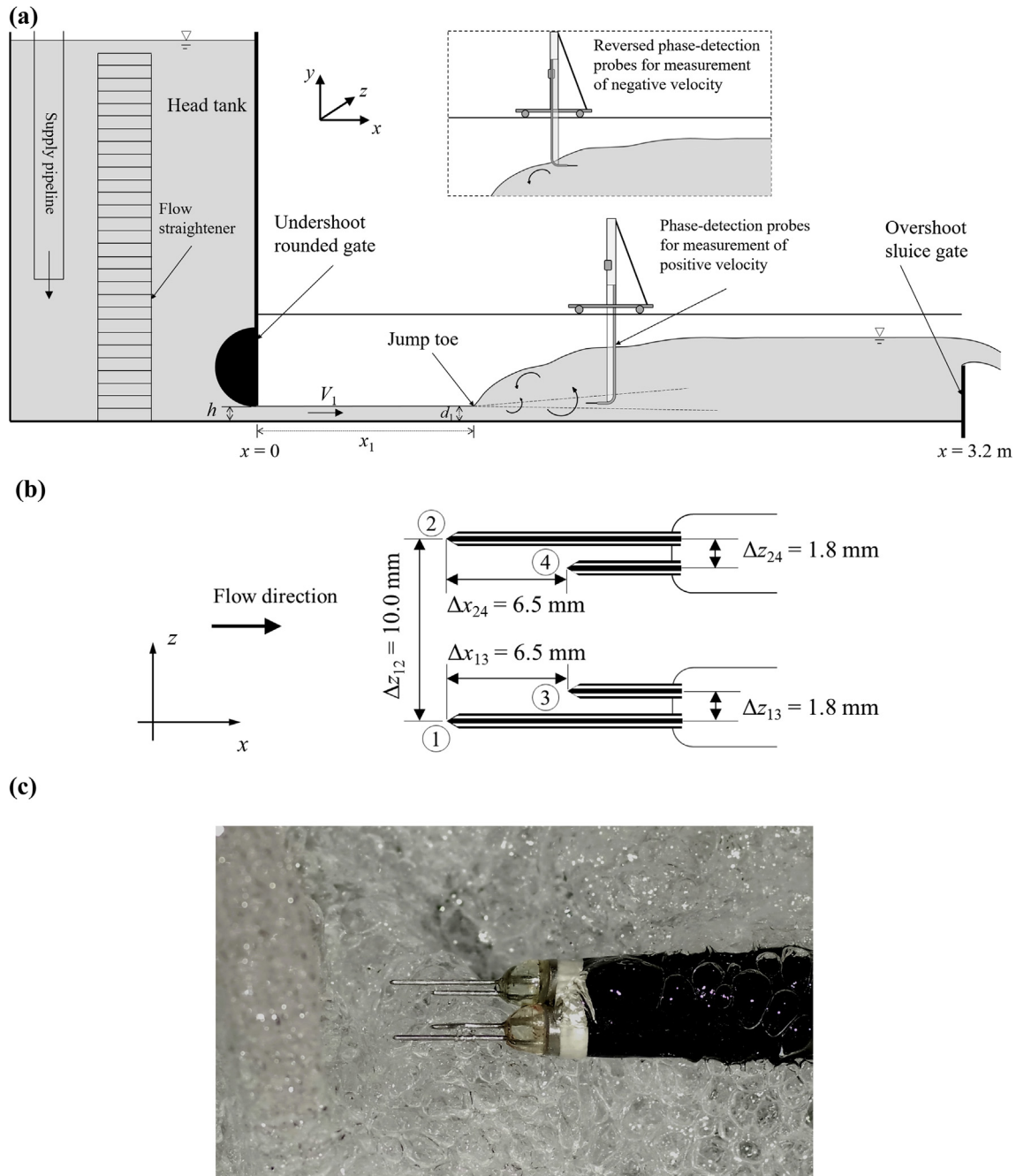
**Fig. 2.** Sketch of experimental channel and phase-detection sensor array configuration: (a) Experimental setup and key parameters to define the flow conditions; (b) Top view sketch of four-tip sensor array. (c) Top view photograph of four-tip sensor array next to the bubbly flow surface.

An array of phase-detection conductivity sensors was used to measure the two-phase flow properties and the turbulent air-water interface motions. The needle-shaped sensors discriminate between air and water phases based on the different electrical resistance of air and water. A detection of air-water interface on the sensor tip leads to a simultaneous voltage change in the probe signal. A simultaneous sampling of two sensors enables derivation of time-averaged air-water interfacial velocity in the direction between the sensor tips. A number of physical data demonstrated that, in high-velocity free-surface flows, the gas-liquid flows behave as a quasi-homogenous mixture within the flow region with void fraction less than 90%, and the two phases travel with a nearly identical velocity, the slip velocity being negligible [12]. A four-tip sensor array was adopted in the present study. Fig. 2B and C shows the sensor array configuration. The four needle sensors, numbered from

1 to 4, were identically manufactured with silver inner-electrodes ($\emptyset$ = 0.25 mm) and stainless-steel outer-electrodes ($\emptyset$ = 0.8 mm). Previous studies on air-water shear flow using finer sensors indicated a majority of bubbles with chord lengths greater than 0.3 mm (e.g. [7]), thus the present sensor size was deemed to be capable to detect most bubbles and have no effect on interfacial velocity quantification. The four sensors were placed in a horizontal $x$-$z$ plane, aligned parallel to each other and all against the inflow direction, with identical elevations $y$ above the invert. The tips of Sensors 1 and 2 had the same longitudinal position $x$ and were separated by a transverse distance $\Delta z_{12}$, with Sensor 1 on the channel centreline ($z = 0$). The relative sensor positions are specified in Fig. 2B. All sensors were excited simultaneously and sampled at 20 kHz per sensor for 45 s at each measurement location. An earlier array configuration was tested and it is discussed in the

**Table 1**
Experimental flow conditions.

| $Q$ (m³/s) | $h$ (m) | $x_1$ (m) | $d_1$ (m) | $V_1$ (m/s) | $Fr$ (–) | $Re$ (–) | Instrumentation |
|---|---|---|---|---|---|---|---|
| 0.0175 | 0.012 | 0.50 | 0.013 | 2.69 | 7.5 | $3.5 \times 10^4$ | Ultra-high-speed video camera |
| 0.0347 | 0.020 | 0.83 | 0.021 | 3.37 | 7.5 | $6.8 \times 10^4$ | Phase-detection probe array |
| 0.0705 | 0.030 | 1.25 | 0.033 | 4.27 | 7.5 | $1.4 \times 10^5$ | Phase-detection probe array |

Appendix A. A trolley system provided support to the phase-detection probes (Fig. 2A). The vertical translation of the probes were monitored by a digimatic scale unit within an accuracy of ± 0.025 mm. In the upper part of the jump roller, the disturbance of the probe support structures on the measurement of reversing flow was evaluated by pointing the probe sensors downstream (Fig. 2A). Further details were reported in Wang and Chanson [36].

A total of three hydraulic jump conditions were investigated for the same inflow Froude number $Fr = 7.5$ but different inflow aspect ratios $h/W = 0.024$, 0.04 and 0.06, where $h$ is the upstream gate opening and $W$ is the channel width (Fig. 2A). The corresponding Reynolds numbers were $Re = 3.5 \times 10^4$, $6.8 \times 10^4$ and $1.4 \times 10^5$ respectively. A constant ratio of the inflow length to upstream gate opening $x_1/h = 41.5$ corresponded to partially-developed inflow conditions. The smallest Reynolds number was only tested using an optical flow technique to demonstrate the two-dimensional velocity field in the $x$-$y$ plane against the channel sidewall. Air-water flow measurements were undertaken for the two larger Reynolds numbers, in several vertical cross-sections along the centreline of hydraulic jump roller. Table 1 summarises the flow conditions, where $V_1$ is the average inflow velocity at $x = x_1$: i.e. $V_1 = Q/(W \times d_1)$.

Notes: $Q$ flow rate, $h$ upstream gate opening, $x_1$ longitudinal jump toe position, $d_1$ inflow depth, $V_1$ average inflow velocity, $Fr$ inflow Froude number, $Re$ inflow Reynolds number.

## 3. Data processing

### 3.1. Time-averaged interfacial velocity and turbulence intensity

A correlation between the signals of two phase-detection sensors provides some information about the average air-water interfacial transport between the sensor tips [15]. Let us define $R_{ij}(\tau)$ as the cross-correlation function between the signals of sensors $i$ and $j$, where $i,j = 1, 2, 3, 4$ and $\tau$ is the signal time lag. When the same amount of air-water fluid is detected in turn by Sensors $i$ and $j$, the cross-correlation function exhibits a maximum correlation coefficient $R_{ij,max}$ at a time lag $\tau = T_{ij}$, i.e. $R_{ij}(T_{ij}) = R_{ij,max}$. Then the time scale $T_{ij}$ represents the average interfacial travel time between the sensors tips $i$ and $j$. The time-averaged interfacial velocity component is

$$V_{ij} = \frac{\sqrt{\Delta x_{ij}^2 + \Delta z_{ij}^2}}{T_{ij}} \tag{1}$$

where $\Delta x_{ij}$ and $\Delta z_{ij}$ are the longitudinal and transverse separation distances between Sensors $i$ and $j$. For the sensor array configuration in Fig. 2B, the longitudinal velocity is measured between Sensors 1 and 3, as well as between Sensors 2 and 4, assuming $\Delta z_{13} = \Delta z_{24} \approx 0$. The transverse velocity is measured between Sensors 1 and 2, as well as between Sensors 3 and 4. Physical and geometrical considerations further suggest the following relationships:

$$V_{13} \approx V_{24} \approx V_x \tag{2}$$

$$V_{12} \approx V_{34} \approx V_z \tag{3}$$

$$V_{23} = \sqrt{V_{13}^2 + V_{12}^2} \approx V_{14} = \sqrt{V_{24}^2 + V_{12}^2} \approx \sqrt{V_x^2 + V_z^2} \tag{4}$$

where $V_x$ and $V_z$ are the time-averaged interfacial velocity components in the longitudinal and transverse directions respectively.

For $i = j$, the correlation function $R_{ii}(\tau)$ becomes the auto-correlation function of the signal of Sensor $i$. Defining the auto-correlation time scale $t_{ii}$ and cross-correlation time scale $t_{ij}$ as

$$t_{ii} = \int_0^{\tau(R_{ij}=0)} R_{ii}(\tau)d\tau \tag{5}$$

$$t_{ij} = \int_{T_{ij}}^{\tau(R_{ij}=0)} R_{ij}(\tau)d\tau \tag{6}$$

the interfacial turbulence intensity $Tu_{ij} = v_{ij}'/V_{ij}$ can be approximated as [13]

$$Tu_{ij} = \frac{\sqrt{2}}{\sqrt{\pi}\,|T_{ij}|} \sqrt{\left(\frac{t_{ij}}{R_{ij,max}}\right)^2 - t_{ii}^2} \tag{7}$$

Eq. (7) is derived based upon some key assumptions, including assuming a random detection of infinitely large number of air-water interfaces. The assumption implies the auto-correlation and cross-correlation functions following a Gaussian distribution, for which the standard deviations can be expressed using the characteristic time scales $t_{ii}$ and $t_{ij}$ [11]. It is noteworthy that, in the presence of large-scale turbulent structures, bubbles are grouped in clusters, and the detection of air-water interfaces may not be a true random process. Further, the turbulence intensity $Tu_{ij}$ is a spatial average value over the distance between two sensor tips, thus is affected by the sensor separation distance. The standard deviation of interfacial velocity component is thus calculated as

$$v_{ij}' = \frac{\sqrt{2(\Delta x_{ij}^2 + \Delta z_{ij}^2)}}{\sqrt{\pi}\,|T_{ij}|^2} \sqrt{\left(\frac{t_{ij}}{R_{ij,max}}\right)^2 - t_{ii}^2} \tag{8}$$

### 3.2. Characteristic transverse velocity component

In a quasi-two-dimensional flow, the longitudinal interface convection is detected by Sensors 1 and 2 at the same longitudinal position ($\Delta x_{12} = 0$). For signals consisting of a sufficiently large amount of samples, the maximum cross-correlation coefficient $R_{12,max}$ is achieved for a zero time lag: i.e. $T_{12} \approx 0$, providing no information on the time-averaged transverse motion. A correlation analysis may reveal the instantaneous transverse interface motion only when the signal sampling duration is reasonably small, so that the information related to the transverse motion is not "overwritten" by that of the mean streamwise motion. Such a signal length should be comparable to or slightly larger than the time scale of the interface motion between the two sensors, thus is relevant to the sensor separation distance $\Delta z_{12}$. While a too small time interval might not cover a sufficient amount of air-water interfaces, a too large interval would contain too many interfaces belonging to multiple opposite motions and give an average transverse velocity being infinitely large (i.e. $T_{12} \approx 0$ in Eq. (1)).

Herein a signal segment with time interval $\Delta t = 0.2$ s was selected to characterise the transverse interfacial motion for a sensor separation distance $\Delta z_{12} = 10$ mm. Fig. 3A shows a cross-correlation function between two 0.2 s signal segments recorded by Sensors 1 and 2. The correlation coefficient $R_{12}$ is plotted as a function of the ratio of sensor separation $\Delta z_{12}$ to time lag $\tau$. Despite the relatively small sample size, the peaks in correlation function might indicate some characteristic transverse velocities. Herein the local maximum correlation coefficients
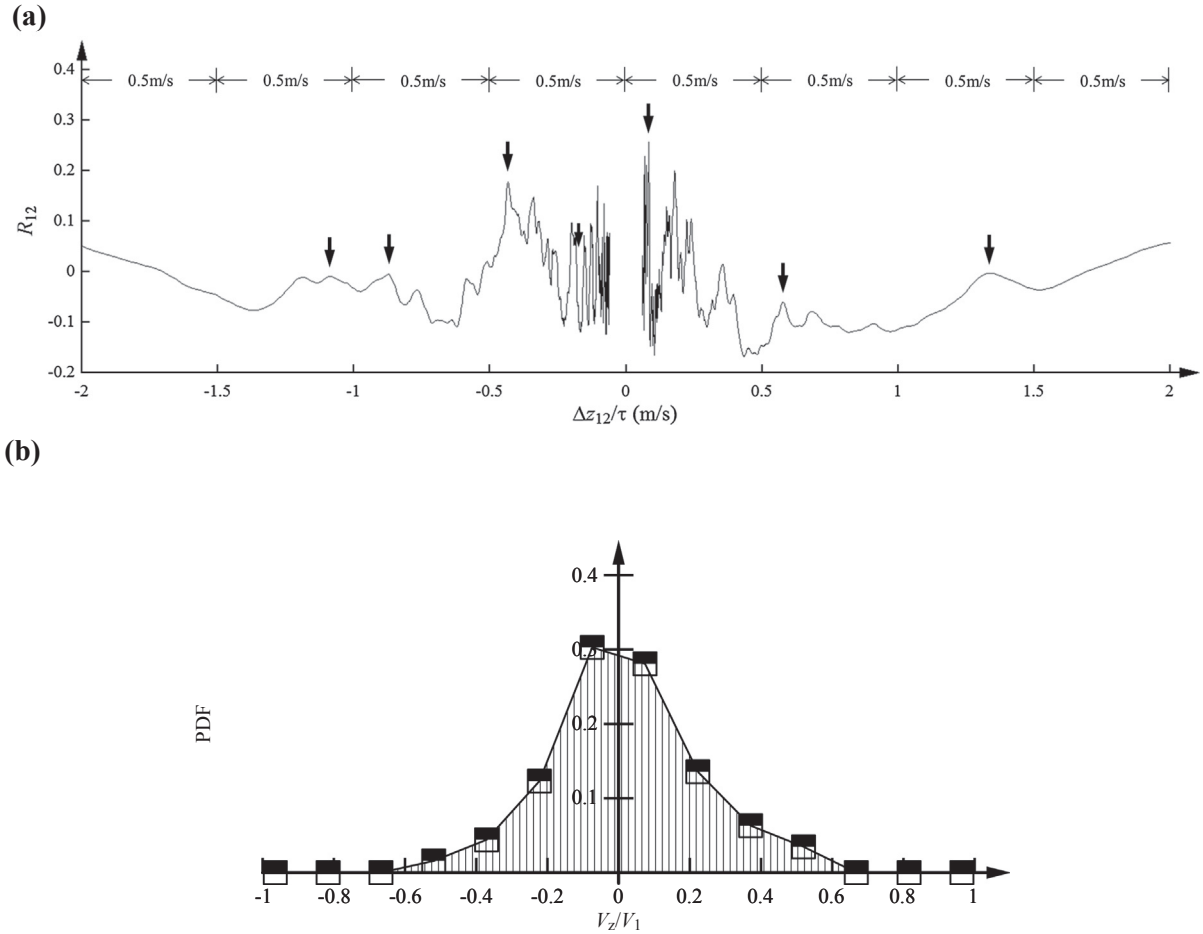
**(a)**



**(b)**



**Fig. 3.** Instantaneous transverse velocity samples. Flow conditions: $Q = 0.0347\ \mathrm{m^3/s}$, $x_1 = 0.83\ \mathrm{m}$, $d_1 = 0.021\ \mathrm{m}$, $Fr = 7.5$, $Re = 6.8 \times 10^4$, $x\text{-}x_1 = 0.25\ \mathrm{m}$, $y = 0.036\ \mathrm{m}$. (a) Cross-correlation function between two 0.2 s signal segments recorded with 10 mm transverse sensor separation distance. Arrows indicate maximum correlation coefficients in every 0.5 m/s velocity bin; (b) Probability density function of transverse velocity samples.

were collected for every 0.5 m/s velocity bin between $\Delta z_{12}/\tau = -5\ \mathrm{m/s}$ and 5 m/s, as indicated by arrows in Fig. 3A. For the entire 45 s signal, a total of 50 non-overlapping 0.2 s long signal segments were analysed, giving 120–300 characteristic velocities between $-5\ \mathrm{m/s}$ and 5 m/s. The probability distributions of these transverse velocities exhibited a normal distribution, with the average being zero (Fig. 3B). The characteristic instantaneous transverse velocity magnitude was determined by the average of all these velocity samples weighted by the corresponding local maximum correlation coefficients:

$$|V_z| = \frac{\sum_1^N ((R_{12,\max})_n |(V_z)_n|)}{\sum_1^N (R_{12,\max})_n} \tag{9}$$

The standard deviation of the data set weighted by the correlation coefficients provided the measure of transverse velocity fluctuations, and its ratio to $|V_z|$ characterised a turbulence intensity $Tu_z$. Note that $Tu_z$ could not be approximated by Eq. (7) because the small data size of transverse velocity samples was in disagreement with the assumptions underlying Eq. (7).

Importantly the characteristic transverse velocity $|V_z|$ was obtained for a given sensor separation $\Delta z_{12} = 10\ \mathrm{mm}$ and time interval $\Delta t = 0.2\ \mathrm{s}$. The results were affected by both the length and time scales, and the impacts are illustrated in Fig. 4. Some small transverse velocities were only recorded for small distances $\Delta z_{12}$ or short time intervals $\Delta t$, because of the small size or short "lifetime" of the bubbly structures moving or oscillating transversely. These small turbulent structures were not detected by both sensors when $\Delta z_{12}$ was larger than their largest transverse displacement (Fig. 4A). On the other hand, a longer

sample duration tended to include more information of the streamwise flow, which reduced the time lag between the signals thus yielded a larger average velocity (Fig. 4B).

### 3.3. Reynolds shear stress calculations

A total of six characteristic velocity fluctuations may be estimated for a four-sensor array, and the following relationships should hold

$$v'_{13} \approx v'_{24} \approx v'_x \tag{10}$$

$$v'_{12} \approx v'_{34} \approx v'_z \tag{11}$$

$$v'_{23} = \sqrt{v'^2_{13} + v'^2_{12} + 2(v_{13}v_{12})'} \approx v'^2_{14} = \sqrt{v'^2_{24} + v'^2_{12} + 2(v_{24}v_{12})'} \tag{12}$$

Physically, the terms $v'^2_{23}$ and $v'^2_{14}$ are proportional to a combination of normal and tangential Reynolds stresses. Eq. (1) may provide an indirect means to estimate the tangential Reynolds stress component:

$$(v_x v_z)' \approx \frac{1}{2}(v'^2_{23} - v'^2_x - v'^2_z) \tag{13}$$

where $v_{23}'$ (or $v_{14}'$) was measured between phase-detection Sensors 2 and 3 (or between Sensors 1 and 4), $v_{23}'$ (or $v_{14}'$) and $v_x'$ were calculated by Eq. (7) and $v_z'$ was directly given by the standard deviation of transverse velocity samples weighted by corresponding correlation coefficients, as defined above.
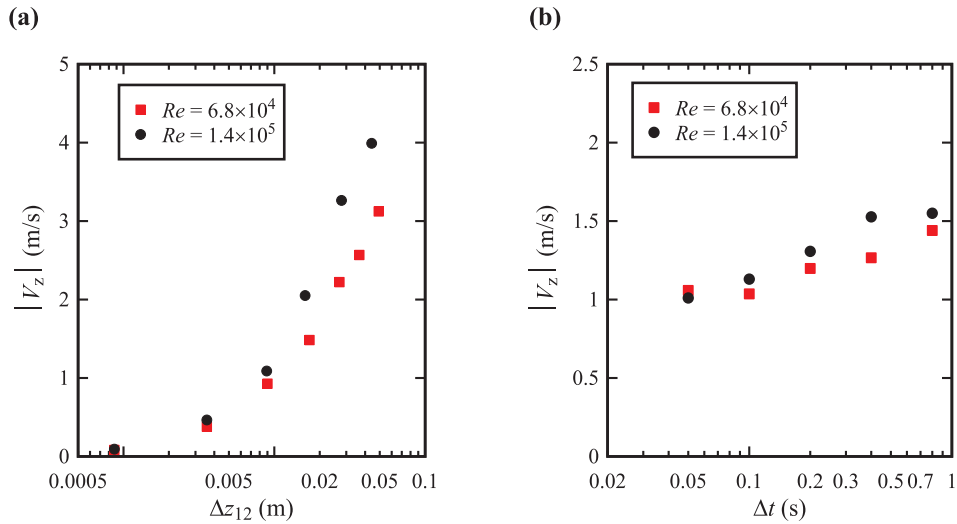
**(a)**

**(b)**



**Fig. 4.** Impact of spatial sensor separation and signal segment duration on quantification of transverse velocity magnitude in lower jump roller. (a) Effect of transverse sensor separation distance for time interval of 0.2 s. (b) Effect of signal segment time interval for sensor separation of 10 mm.

## 4. Results

### 4.1. Presentation

For an inflow Froude number $Fr = 7.5$, the hydraulic jumps were characterised with a marked bubbly roller (Fig. 1B). That is, while the impinging flow sustained a relatively high velocity near the channel bed, flow recirculation took place next to the free-surface, with spray and splashing projected in air. A shear layer formed between the bottom boundary layer ($V_x > 0$) and the reversing flow region ($V_x < 0$) due to the large velocity gradient from positive to negative. Fig. 5 depicts the optical flow field in the vertical plane against the channel sidewall, for a relatively small Reynolds number. The velocity vectors were calculated based on a pixel density analysis of high-speed video optical flow. The time-averaged velocity distribution over the 1.5 s recording duration showed clearly the boundary between the positive and negative velocity regions. While the high-speed jet core was decelerated in the streamwise direction, the recirculating velocity magnitude in the upper roller appeared to be constant over the first two-thirds of the roller length.

### 4.2. Air-water flow longitudinal velocity distributions

A substantial amount of air was entrained into the shear layer at the jump toe. The formation of the shear layer and the entrainment of air were observed together with successive downstream ejection of large-size vortices. Bubbles were advected in the vortices and interacted with turbulent structures of different length and time scales.

Using the phase-detection sensor array, the time-averaged void fraction $C$ was recorded simultaneously at four sensor tips, whereas the longitudinal time-averaged interfacial velocity $V_x$ and turbulence intensity $Tu_x$ were measured at two side-by-side transverse locations, one on the channel centreline between Sensors 1 and 3 ($z/W = 0$) and the other at $\Delta z = 10$ mm apart between Sensors 2 and 4 ($z/W = 0.02$). The results are presented in Fig. 6 for the same flow conditions ($Fr = 7.5$, $Re = 1.4 \times 10^5$). In Fig. 6, the roller free-surface is plotted at an elevation $y = Y_{90}$ where $C = 0.9$. The time-averaged void fraction showed a bell-shape distribution in the turbulent shear layer and a monotonically increasing distribution across the free-surface region (Fig. 6A). The longitudinal velocity showed a similar distribution to that in Fig. 5, although the Reynolds number was one order of magnitude higher and the transverse location was on the channel centreline rather than next to the sidewall (Fig. 6B). In the positive velocity region, a maximum velocity was seen at the outer edge of bottom boundary layer, decreasing in the longitudinal direction. The negative velocity data were somehow scattered because of the impact of free-surface fluctuations. It is also noteworthy that the velocity measurement with phase-detection probes in the free-surface region was not free of influence of vertical velocity component driven by gravity. The detection of vertical velocity component by horizontally positioned probe sensors tended to broaden the correlation function between the sensor signals as well as to enlarge the velocity estimate. This can be seen by comparing Figs. 5 and 6B in
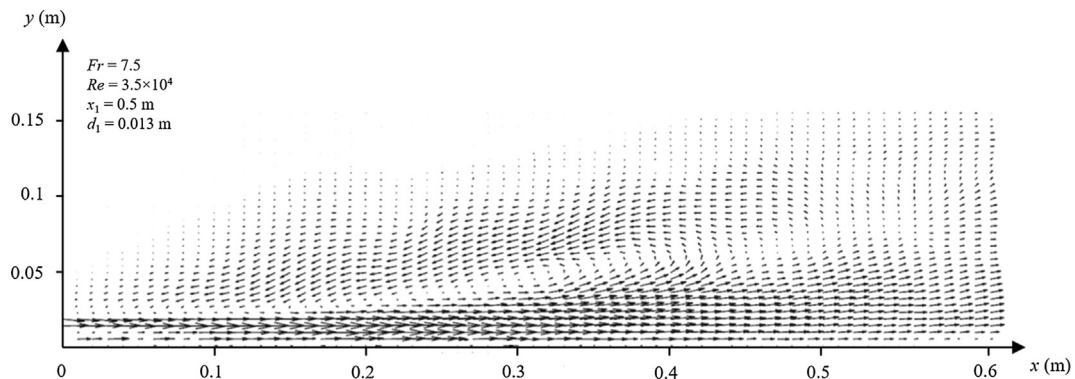


**Fig. 5.** Two-dimensional optical flow field in a vertical visualisation plane next to the channel sidewall. Flow conditions: $Q = 0.0175$ m³/s, $x_1 = 0.5$ m, $d_1 = 0.013$ m, $Fr = 7.5$, $Re = 3.5 \times 10^4$.
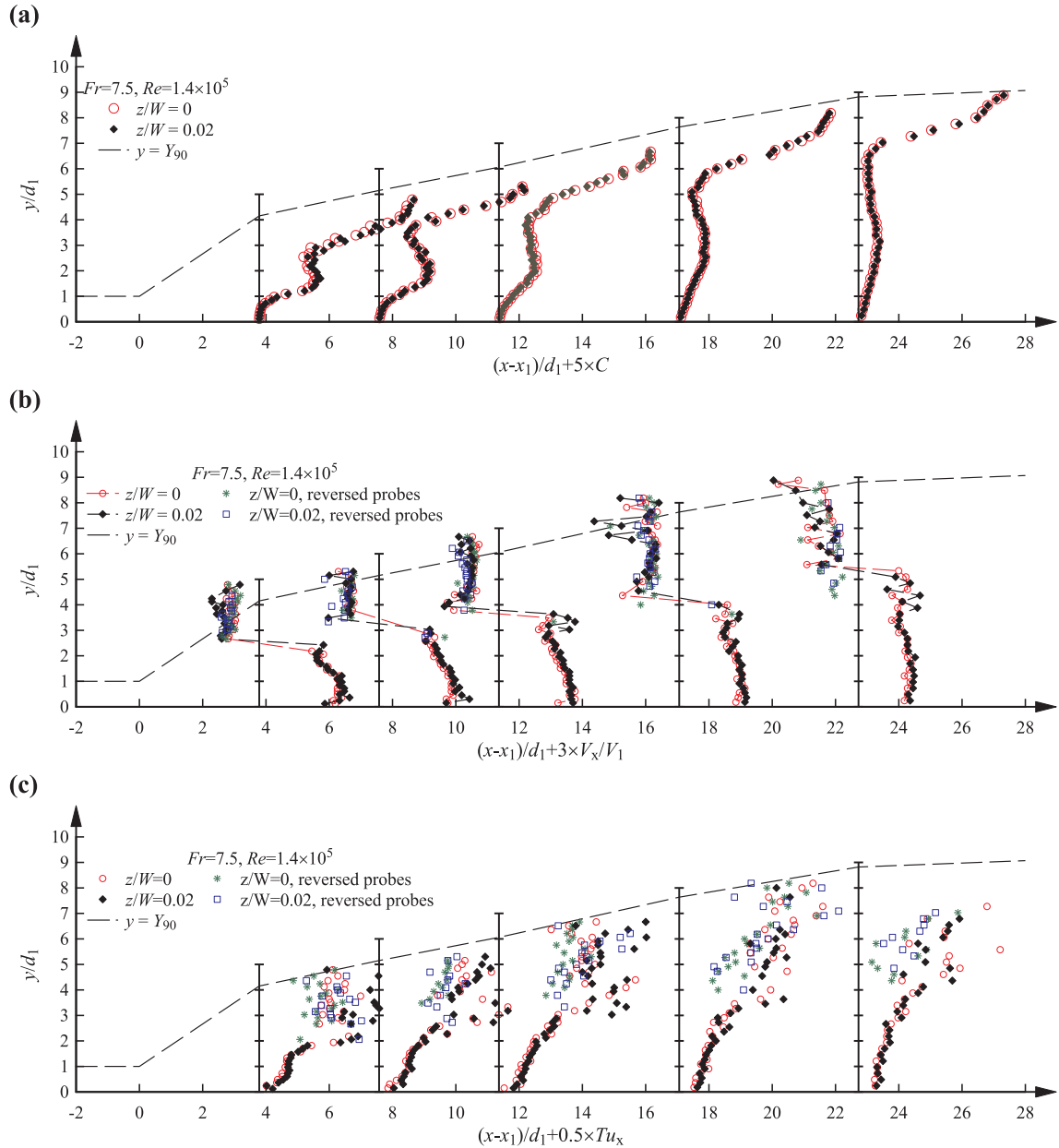
**(a)**



**(b)**



**(c)**



**Fig. 6.** Longitudinal time-averaged air–water flow properties measured at side-by-side transverse locations. (a) Void fraction measured with single phase-detection sensor. (b) Interfacial velocity. (c) Interfacial turbulence intensity.

terms of the velocity data in the spray region above the roller surface. The interference of the phase-detection probe support structures on the measurement of reversing flow was further investigated by comparing the results of probes with opposite orientations in the recirculation region. In terms of interfacial velocity, little difference was seen between the opposite probe orientations (Fig. 6B), implying negligible impact of the wake of probe support structures on velocity quantification. This conclusion only applies to the free-surface reversing flow driven by gravity, excluding the shear flow region underneath.

The interfacial turbulence intensity calculated with Eq. (7) increased with increasing elevation from the bottom across the positive velocity region, and became large and scattered in the negative velocity region, because of the large-scale free-surface deformations and broadened correlation function between probe signals (Fig. 6C) [37]. A reversed probe position gave quantitatively comparable values in the recirculation region, though the results were generally less scattered and slightly lower in average magnitude. This turbulence intensity

should be treated with great care, keeping in mind of the dominant impact of low-frequency flow motions [37]. All parameters (Fig. 6A–C) showed close values at the side-by-side locations ($z/W = 0$ & 0.02), confirming the time-averaged two-dimensional flow pattern for the period of 45 s sampling duration. The longitudinal evolutions of the data profiles reflected the flow de-aeration and deceleration processes, as well as the turbulence dissipation at downstream end of the roller. The typical data distributions were consistent with the findings of Murzyn and Chanson [27], Chachereau and Chanson [5] and Wang and Chanson [35].

### 4.3. Characteristic transverse velocity and velocity fluctuations

The characteristic transverse velocity component $|V_z|$ was obtained for a sensor separation distance $\Delta z_{12} = 10$ mm and a typical sampling duration $\Delta t = 0.2$ s. The results are presented in Fig. 7 in dimensionless form for two Reynolds numbers, each at five vertical cross-sections, and
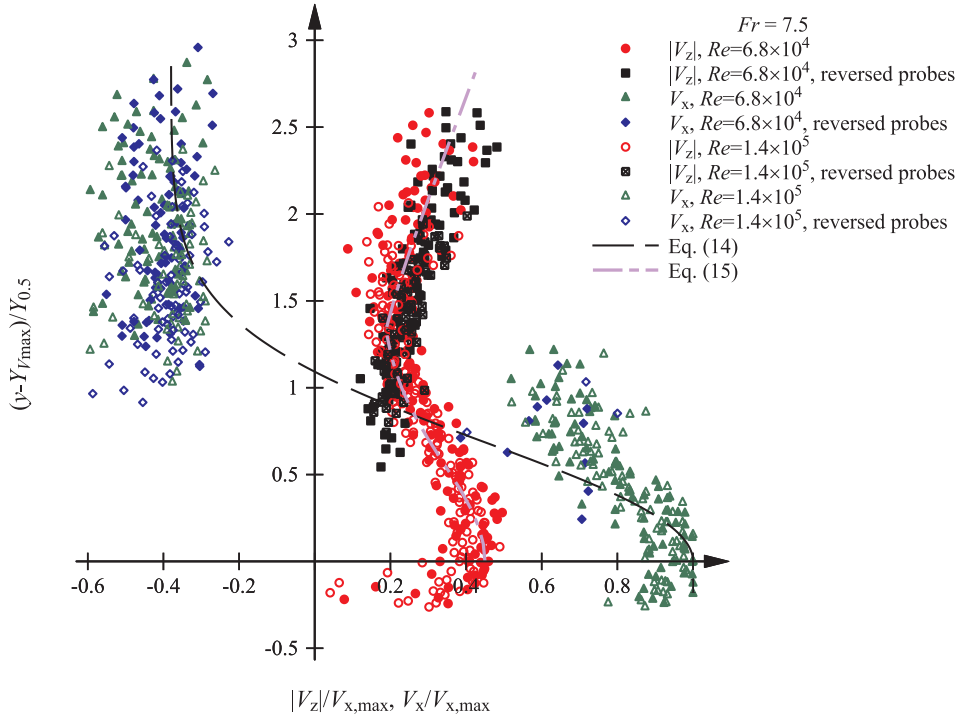
for both normal and reversed probe orientations. The longitudinal velocity component $V_x$ is included for comparison. Note that the instantaneous transverse velocity could be in either positive ($+z$) or negative ($-z$) direction, the average being zero. Herein $|V_z|$ represents an average transverse velocity amplitude.

In Fig. 7, both longitudinal and transverse velocity data exhibited spatial self-similar distributions, and the orientation of phase-detection probe array had little effects on velocity measurements in the recirculation region. The longitudinal velocity data were compared with the solution of wall jet equation [8,31]

$$\frac{V_x - V_{x,\text{recirc}}}{V_{x,\text{max}} - V_{x,\text{recirc}}} = \exp\left(-\frac{1}{2}\left(1.765\frac{y - Y_{V_{\text{max}}}}{Y_{0.5}}\right)^2\right) \quad y > Y_{V\,max} \tag{14}$$

where $V_{x,\text{max}}$ is the maximum longitudinal velocity observed at the elevation $Y_{V\text{max}}$, $V_{x,\text{recirc}}$ is the average recirculation velocity, $V_{x,\text{recirc}}/V_{x,\text{max}} = -0.38$ herein, and $Y_{0.5}$ is the vertical position where $V_x = V_{x,\text{max}}/2$. In the shear flow region with $V_x > 0$, the results showed similar profile shapes between the transverse and longitudinal velocity components. A maximum transverse velocity amplitude was also seen at the outer edge of bottom boundary layer, the ratio of transverse to longitudinal velocity maxima being mostly between $|V_z|/V_x = 0.4$ and 0.5. In the upper free-surface region, the ratio $|V_z|/|V_x|$ approached gradually to unity with increasing elevation as well as increasing void fraction. Interestingly, this finding might be comparable to the finding of Wang and Murzyn [38] in terms of integral turbulent length scale, which also showed a transverse to longitudinal ratio $L_Z/L_X < 1$ in the shear flow and $L_Z/L_X \sim 1$ near the free-surface. These findings suggested a stretched flow structure in the lower part of jump roller, related to the shear flow motion overwhelmingly driven by the streamwise inertia force, whereas the dominant role of gravity led to more homogeneous recirculation structures in the upper roller. The transverse velocity data in Fig. 7 may be approximated as

$$\frac{|V_z| - \alpha V_{x,\text{recirc}}}{V_{x,\text{max}} - V_{x,\text{recirc}}} = \alpha \exp\left(-\frac{1}{2}\left(1.765\frac{y - Y_{V_{\text{max}}}}{Y_{0.5}}\right)^2\right) \quad y > Y_{V\,max} \tag{15a}$$

where

$$\alpha = \begin{cases} 0.45 & \text{for } 0 < (y - Y_{V_{\text{max}}})/Y_{0.5} < 1.3 \\ 0.45(y - Y_{V_{\text{max}}})/Y_{0.5} - 0.15 & \text{for } (y - Y_{V_{\text{max}}})/Y_{0.5} > 1.3 \end{cases} \tag{15b}$$

Overall, for a physical measurement at a length scale $\sim 10^{-2}$ m and time scale no larger than 0.2 s, a typical velocity of the instantaneous transverse interfacial motion was about half of the time-averaged longitudinal velocity in the shear flow and of the same order of magnitude close to the roller surface.

The relationships predicted by Eq. (4) were checked against the longitudinal and transverse velocity components, $V_x$ and $V_z$, and the velocity vector $V_{23}$ measured between Sensors 2 and 3 (and $V_{14}$ between Sensors 1 and 4). Fig. 8 shows a comparison between the direct
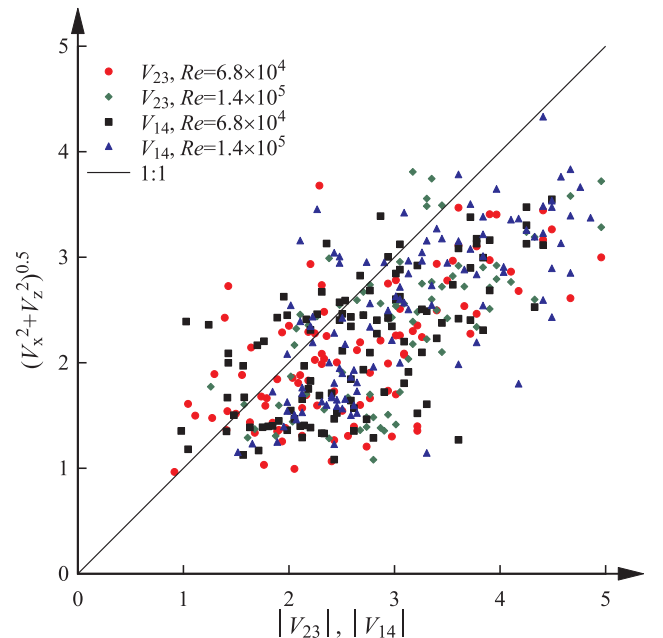


**Fig. 8.** Comparison between velocity vectors measured with phase-detection sensors and calculated with longitudinal and transverse components.
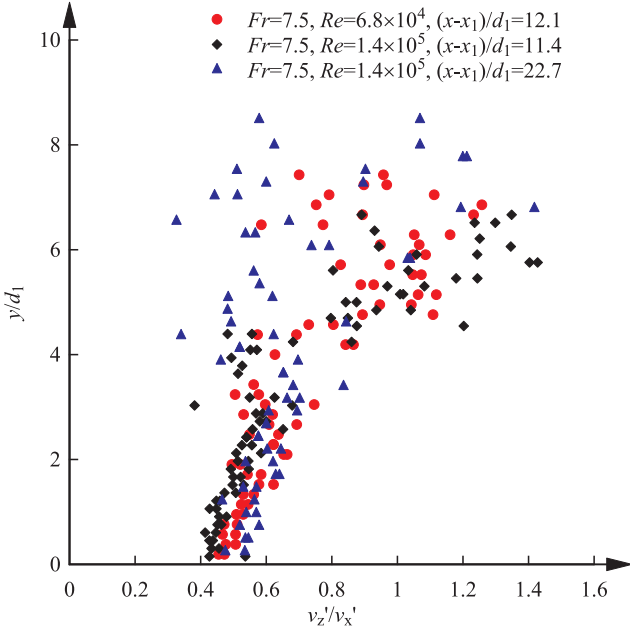
**Fig. 9.** Vertical distributions of ratio $v_z'/v_x'$ of transverse to longitudinal velocity fluctuations.

vertical cross-sections. The data showed similar data distributions. Note that $v_z'$ and $v_x'$ were obtained at different time scales. In the turbulent shear flow where the longitudinal turbulence intensity $Tu_x$ was less scattered (see Fig. 6C), the ratio $v_z'/v_x'$ increased gradually from between 0.4 and 0.5 to between 0.6 and 0.7 with increasing vertical position. In the upper roller region, despite the data scattering in $v_x'$, the velocity fluctuation magnitudes $v_z'$ and $v_x'$ appeared to be quantitatively comparable. An overall increasing trend was shown for the ratio $v_z'/v_x'$ with increasing distance from the bottom to free-surface. The turbulence intensity $Tu_z = v_z'/|V_z|$ had an average value of 1 across the vertical cross-sections. Resch and Leutheusser [33] measured both longitudinal and transverse velocity fluctuations in the roller using a double V-shaped hot-film probe for $Fr = 6$. Their data showed a marked maximum transverse velocity fluctuation $v_z'/V_1 \approx 0.15$ and maximum longitudinal velocity fluctuation $v_x'/V_1 \approx 0.3$ in the turbulent shear layer, $V_1$ being the average inflow velocity. The finding was consistent with the present results in terms of ratio $v_z'/v_x'$, although the magnitudes of turbulence intensities were smaller, because Resch and Leutheusser [33] recorded the continuous water velocity and turbulence, whereas the present study recorded the velocity and turbulence of consecutive air-water interfaces. Indeed, the interfacial turbulence estimate based on correlation analysis (e.g. Eq. (7)) was affected by the large-scale motions of the roller, particularly next to the fluctuating roller free-surface [37]. Therefore, the approximation of interfacial turbulence intensity was subject to some uncertainty and often overestimated.

## 5. Discussion

### 5.1. Reynolds stresses

Dimensionless Reynolds stresses were calculated for the corresponding velocity fluctuations, namely, the longitudinal normal Reynolds stress $\rho(1-C)v_x'^2/(0.5\rho V_1^2)$, the transverse normal Reynolds stress $\rho(1-C)v_z'^2/(0.5\rho V_1^2)$, and the tangential Reynolds stress $\rho(1-C)(v_xv_z)'/(0.5\rho V_1^2)$, where $\rho$ is the water density and $C$ the void fraction of air-water flow. Typical results are shown in Fig. 10. The present data yielded dimensionless normal Reynolds stresses between 0.1 and 0.3 in the transverse direction, one order of magnitude smaller than in the longitudinal direction. The tangential Reynolds stress data were
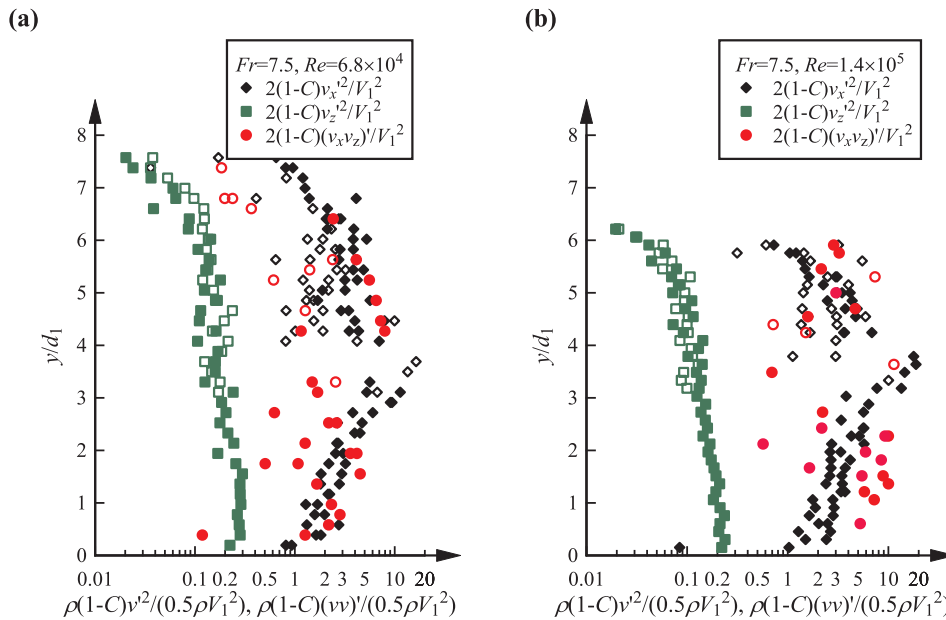
measurement results (horizontal axis) and calculation results (vertical axis). The bias of the point distributions from the 1:1 line was attributed to the scattering velocity data measured between probe Sensors 1 and 4 or between Sensors 2 and 3. The quality of time-averaged turbulence data deteriorated significantly when the phase-detection sensors were not aligned along the main flow direction. It is also noteworthy that $V_x$ was a time-averaged velocity whereas $V_z$ was a characteristic instantaneous velocity. Therefore, the sum of the vectors should be considered at the smaller time scale, i.e. 0.2 s herein, compared to the directly measured velocities derived from 45 s long samples. Nevertheless, the data showed calculation and measurement results in the same order of magnitude.

The ratio $v_z'/v_x'$ was calculated, with the longitudinal velocity fluctuation $v_x'$ given by Eq. (8). The results are shown in Fig. 9 for three

**(a)**

**(b)**



**Fig. 10.** Vertical distributions of normal and tangential Reynolds stresses. Hollow symbols stand for data collected with reversed phase-detection probe array with sensors pointing downstream. (a) $Fr = 7.5$, $Re = 6.8 \times 10^4$, $(x-x_1)/d_1 = 12.1$. (b) $Fr = 7.5$, $Re = 1.4 \times 10^5$, $(x-x_1)/d_1 = 11.4$.

approximated in the same order of magnitude as the longitudinal normal stress based on Eq. (13). Such values were unusually large because, in Eq. (13), the terms $v_{23}'$ (or $v_{14}'$, see sketch in Fig. 2B) were sometimes large, scattered and physically meaningless. The unsuccessful quantification of $v_{23}'$ (or $v_{14}'$) was associated with the complex flow structures that led to broadened and sometimes biased cross-correlation functions between the probe signals. For comparison, Resch and Leutheusser [33] measured the water-phase Reynolds stresses, giving dimensionless tangential stress $(v_x v_z)'/V_1^2$ in the order of $10^{-2}$, while the longitudinal stress $v_x'^2/V_1^2$ was in the order of $10^{-1}$. The validity of Reynolds stress estimate may be further tested in more organised air-water flows with lesser flow recirculation and instabilities.

### 5.2. Uncertainties of measurement and limitation in data processing method

The derivation of turbulence properties using phase-detection probe signals had intrinsic limitations associated with the statistical nature of cross-correlation technique. The application of cross-correlation technique required a relatively high interfacial velocity with a constant flow direction. This was not satisfied in the transition region between positive and negative velocity flows in hydraulic jump roller as well as next to the roller free-surface, leading to bias in time-averaged velocity (see comparison between Figs. 5 and 6B) and turbulence intensity.

The present method to characterise the velocity fluctuations other than in the longitudinal direction showed uncertainties related to the complexity and anisotropy of the flow and the statistical consideration in data processing. First the small signal segment ($\Delta t = 0.2$ s) contained a limited number of air-water interfaces, and the corresponding cross-correlation function might exhibit random and biased peaks (e.g. Fig. 3A). The bias could not be minimised using segment-averaged correlation functions because the average velocity was zero. Instead, characteristic velocities corresponding to local peak correlation coefficients were recorded for each signal segment and the average velocity amplitude $|V_z|$ weighted by the correlation coefficient was considered. The limited sample size would also affect the estimate of velocity fluctuations given by the sample standard deviation $v_z'$. The uncertainties were also reflected in the calculation of Reynolds stresses.

Second the detection of air-water interfaces recorded a combination of all interface motions, both longitudinally and transversely. A time interval of $\Delta t = 0.2$ s was selected to filter the longitudinal components and to best reflect the possible transverse motions. However, there was no independent means to justify whether the characteristic peaks in correlation functions (e.g. Fig. 3A) corresponded physically to a longitudinal or transverse motion. For a small-size signal segment, it was also possible that a maximum correlation coefficient was given by random detection of irrelevant bubbles at the two sensor tips. The filtering of phase-detection probe signals yielded flow properties dependent upon the size of signal segment (herein $\Delta t = 0.2$ s) as well as the physical sensor separation distance (herein $\Delta z = 10$ mm). Any change in signal segment size or sensor separation distance would affect the derived instantaneous transverse velocity fluctuations. More physical data and/or theoretical consideration are required to support and justify the selection of these parameters.

### A. Four sensor array design

Two arrays of four-point air-water flow measurement were tested. Fig. 11 illustrates the two array configurations, viewed in elevation. The two arrays were identically designed with symmetrical sensor positions and identical sensors, manufactured with silver inner-electrodes (Ø = 0.25 mm) and stainless steel outer-electrodes (Ø = 0.8 mm). The four needle sensors were located within the same x-z plane: i.e., the sensor tips were at identical vertical elevation y above the invert. The leading tips had the same longitudinal positions and were separated by a transverse distance $\Delta z_{12}$. A first series of four-point measurements was conducted with the Configuration I. The Configuration II was later adopted to avoid interference of the longer sensor in the path between the shorter sensor of the same dual-tip probe and the longer sensor of the other probe side by side. Most results in the present study were obtained using the second configuration. Wang and Chanson [36] presented some comparison between the two configurations.

## 6. Conclusion

Four-point air-water flow measurements were performed in highly aerated hydraulic jumps using a phase-detection sensor array. Air-water interfacial velocity and turbulence properties were measured between any two sensors in a horizontal plane, including the longitudinal velocity component and turbulence intensity which were well-documented in previous studies. The air-water flow properties measured at different transverse locations yielded almost the same time-averaged values as a result of the time-averaged two-dimensional flow pattern in a prismatic rectangular channel. The longitudinal velocity distributions measured with phase-detection probes compared favourably with optical flow data. In the upper free-surface recirculation region, little impact of phase-detection probe orientation was observed on velocity and turbulence intensity measurements.

With the four-tip phase-detection sensor array, it was possible to derive the velocity and turbulence intensity components in a direction with an angle of $\tan^{-1}(\Delta z/\Delta x)$ from the longitudinal direction, $\Delta x$ and $\Delta z$ being the longitudinal and transverse separation distances between the sensors. For $\Delta x = 0$, the turbulence properties were obtained in the transverse direction. The statistical cross-correlation analysis had inherent limitations in abstracting information of particle motions other than along the main flow direction. Since the time-averaged transverse velocity equalled zero, a characteristic instantaneous transverse velocity was derived based upon a number of small signal segments. Such a transverse velocity component was the result of a signal filtering for a given length scale (i.e. sensor separation distance) and a time scale (i.e. duration of signal segment). It was expected to provide a measure of the instantaneous transverse motion velocity in the bubbly flow.

For a length scale $\sim 10^{-2}$ m and a time scale no larger than 0.2 s, the typical velocity of instantaneous transverse interfacial motion was about 40–50% of the time-averaged longitudinal velocity in the high-momentum shear flow region, and close to the magnitude of longitudinal velocity component next to the free-surface. The finding was consistent with the different turbulent structures between the lower and upper roller regions. The corresponding transverse velocity fluctuations were about half of that in the longitudinal direction in the shear flow and of the same order of magnitude in the upper recirculation region. The direct measurement of turbulence intensity in a direction apart from the longitudinal direction however lacked accuracy because of the limitation of correlation analysis. The errors were further reflected in the estimate of tangential Reynolds stress. The transverse normal stress was one order of magnitude smaller than the longitudinal normal stress.
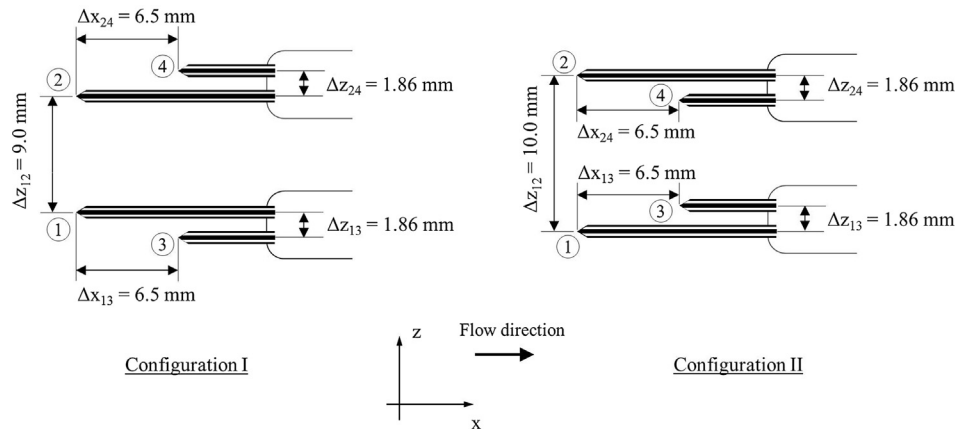
**Fig. 11.** Phase-detection sensor arrays, viewed in elevation.

# References

[1] C. Boyer, A.M. Duquenne, G. Wild, Measuring techniques in gas-liquid and gas-liquid-solid reactors, Chem. Eng. Sci. 57 (16) (2002) 3185–3215.

[2] D.B. Bung, D. Valero, Image processing for Bubble Image Velocimetry in self-aerated flows, in: Proc. 36th IAHR World Congress, The Hague, The Netherlands, 27 June-3 July, 2015.

[3] D.B. Bung, D. Valero, Optical flow estimation in aerated flows, J. Hydraul. Res. 54 (5) (2016) 575–580.

[4] A. Cartellier, Optical probes for multiphase flow characterization: some recent improvements, Chem. Eng. Technol. 24 (5) (2001) 535–538.

[5] Y. Chachereau, H. Chanson, Bubbly flow measurements in hydraulic jumps with small inflow froude numbers, Int. J. Multiph. Flow 37 (6) (2011) 555–564, https://doi.org/10.1016/j.ijmultiphaseflow.2011.03.012.

[6] Y. Chachereau, H. Chanson, Free-surface fluctuations and turbulence in hydraulic jumps, Exp. Therm Fluid Sci. 35 (6) (2011) 896–909, https://doi.org/10.1016/j.expthermflusci.2011.01.009.

[7] H. Chanson, T. Brattberg, Air-water bubbly flow in free-shear layers, in: Proc. 1996 ASME Fluids Eng. Conf., San Diego, USA, ASME-FED 236(1), 1996, pp. 357–364.

[8] H. Chanson, Convective transport of air bubbles in strong hydraulic jumps, Int. J. Multiph. Flow 36 (10) (2010) 798–814.

[9] H. Chanson, Phase-detection measurements in free-surface turbulent shear flows, J. Geophys. Eng. 13 (2) (2016) S74–S87, https://doi.org/10.1088/1742-2132/13/2/S74.

[10] H. Chanson, T. Brattberg, Experimental study of the air-water shear flow in a hydraulic jump, Int. J. Multiph. Flow 26 (4) (2000) 583–607, https://doi.org/10.1016/S0301-9322(99)00016-6.

[11] H. Chanson, L. Toombes, Air-water flows down stepped chutes: turbulence and flow structure observations, Int. J. Multiph. Flow 28 (11) (2002) 1737–1761, https://doi.org/10.1016/S0301-9322(02)00089-7.

[12] P. Cain, I.R. Wood, Instrumentation for aerated flow on a spillway, J. Hydraul. Div. 107 (HY11) (1981) 1407–1424.

[13] S. Felder, H. Chanson, Triple decomposition technique in air–water flows: application to instationary flows on a stepped spillway, Int. J. Multiph. Flow 58 (2014) 139–153, https://doi.org/10.1016/j.ijmultiphaseflow.2013.09.006.

[14] F.M. Henderson, Open Channel Flow, MacMillan Company, New York, USA, 1966.

[15] R.A. Herringe, M.R. Davis, Detection of instantaneous phase changes in gas-liquid mixtures, J. Phys. E: Sci. Instrum. 7 (1974) 807–812.

[16] O.C. Jones, J.M. Delhaye, Transient and statistical measurement techniques for two-phase flows: a critical review, Int. J. Multiph. Flow 3 (1976) 89–116.

[17] J. Leandro, R. Carvalho, Y. Chachereau, H. Chanson, Estimating void fraction in a hydraulic jump by measurements of pixel intensity, Exp. Fluids 52 (5) (2012) 1307–1318.

[18] J.M. Lennon, D.F. Hill, Particle image velocity measurements of undular and hydraulic jumps, J. Hydraul. Eng., ASCE 132 (12) (2006) 1283–1294.

[19] M. Liu, N. Rajaratnam, D. Zhu, Turbulent structure of hydraulic jumps of low Froude numbers, J. Hydraul. Eng. ASCE 130 (6) (2004) 511–520.

[20] P. Lubin, S. Glockner, H. Chanson, Numerical simulation of air entrainment and turbulence in a hydraulic jump, Colloque SHF, 2009, pp. 109–114.

[21] K. Mao, T. Hibiki, Flow regime transition criteria for upward two-phase cross-flow in horizontal tube bundles, Appl. Therm. Eng. 112 (2017) 1533–1546.

[22] E. Mignot, R. Cienfuegos, Energy dissipation and turbulent production in weak hydraulic jumps, J. Hydraul. Eng., ASCE 136 (2) (2010) 116–121.

[23] S.K. Misra, J.T. Kirby, M. Brocchini, F. Veron, M. Thomas, C. Kambhamettu, The mean and turbulent flow structure of a weak hydraulic jump, Phys. Fluids 20 (2008) 035106.

[24] M. Mortazavi, V. Le Chenadec, P. Moin, A. Mani, Direct numerical simulation of a turbulent hydraulic jump: turbulence statistics and air entrainment, J. Fluid Mech. 797 (2016) 60–94.

[25] M. Mossa, U. Tolve, Flow visualization in bubbly two-phase hydraulic jump, J. Fluids Eng., ASME 120 (March) (1998) 160–165.

[26] A. Mota, A. Ferreira, A. Vicente, P. Sechet, J. Martins, J. Teixeira, A. Cartellier, Customization of an optical probe device and validation of a signal processing procedure to study gas-liquid-solid flows. Application to a three-phase internal-loop gas-lift Bioreactor, Chem. Eng. Sci. 138 (2015) 814–826.

[27] F. Murzyn, H. Chanson, Experimental investigation of bubbly flow and turbulence in hydraulic jumps, Environ. Fluid Mech. 9 (2) (2009) 143–159, https://doi.org/10.1007/s10652-008-9077-4.

[28] F. Murzyn, D. Mouaze, J.R. Chaplin, Optical fibre probe measurements of bubbly flow in hydraulic jumps, Int. J. Multiph. Flow 31 (1) (2005) 141–154.

[29] F. Murzyn, D. Mouaze, J.R. Chaplin, Air-water interface dynamic and free surface features in hydraulic jumps, J. Hydraul. Res. IAHR 45 (5) (2007) 679–685.

[30] P. Novak, V. Guinot, A. Jeffrey, D. Reeve, Hydraulic Modelling – An Introduction: Principles, Methods and Applications, CRC Press, London, UK, 2010.

[31] N. Rajaratnam, The hydraulic jump as a wall jet, J. Hydraulics Div. ASCE 91 (HY5) (1965) 107–132.

[32] F.J. Resch, H.J. Leutheusser, Le ressaut hydraulique: mesure de turbulence dans la région diphasique (The hydraulic jump: turbulence measurements in the two-phase flow region.), La Houille Blanche 4 (1972) 279-293 (in French).

[33] F.J. Resch, H.J. Leutheusser, Reynolds stress measurements in hydraulic jumps, J. Hydraul. Res. 10 (4) (1972) 409–429.

[34] I.A. Svendsen, J. Veeramony, J. Bakunin, J.T. Kirby, The flow in weak turbulent hydraulic jumps, J. Fluid Mech. 418 (2000) 25–57.

[35] H. Wang, H. Chanson, Experimental study of turbulent fluctuations in hydraulic jumps, J. Hydraulic Eng. ASCE 141(7) (2015) 10 pages https://doi.org/10.1061/(ASCE)HY.1943-7900.0001010.

[36] H. Wang, H. Chanson, Velocity field in hydraulic jumps at large Reynolds numbers: development of an array of two dual-tip phase-detection probes, Hydraulic Model Report No. CH100/15, School of Civil Engineering, The University of Queensland, Brisbane, Australia, 76 pages.

[37] H. Wang, S. Felder, H. Chanson, An experimental study of turbulent two-phase flow in hydraulic jumps and application of a triple decomposition technique, Exp. Fluids 55 (7) (2014) 1–18, https://doi.org/10.1007/s00348-014-1775-8.

[38] H. Wang, F. Murzyn, Experimental assessment of characteristic turbulent scales in two-phase flow of hydraulic jump: from bottom to free surface, Environ. Fluid Mech. 17 (1) (2017) 7–25, https://doi.org/10.1007/s10652-016-9451-6.

[39] G. Zhang, H. Chanson, Application of local optical flow methods to high-velocity free-surface flows: validation and application to stepped chutes, Exp. Therm Fluid Sci. 90 (2018) 186–199, https://doi.org/10.1016/j.expthermflusci.2017.09.010.